Tectonics®

RESEARCH ARTICLE
10.1029/2025TC008840

Key Points:

- The 3 Al_2SiO_5 polymorphs developed during seismic faulting in high-grade peraluminous gneiss of the hanging wall of Woodroffe Thrust (WT)
- The polymorphs grew during different stages of the thermal transient associated with frictional melting recorded by pseudotachylytes
- Andalusite indicates that seismic faulting along the WT occurred at ≤15 km depth, that is much shallower than previously thought

Supporting Information:

Supporting Information may be found in the online version of this article.

Correspondence to:

G. Toffol,
giovanni.toffol@unipd.it

Citation:

Toffol, G., Camacho, A., Mancktelow, N., & Pennacchioni, G. (2025). Depth of ancient seismicity along the Woodroffe Thrust (central Australia): Constraints from pseudotachylytes in peraluminous gneisses. *Tectonics*, *44*, e2025TC008840. https://doi.org/10.1029/2025TC008840

Received 24 JAN 2025
Accepted 12 AUG 2025

Author Contributions:

Conceptualization: G. Toffol, A. Camacho, N. Mancktelow, G. Pennacchioni
Data curation: G. Toffol
Formal analysis: G. Toffol
Funding acquisition: G. Pennacchioni
Investigation: G. Toffol, A. Camacho, G. Pennacchioni
Methodology: G. Toffol
Supervision: A. Camacho, G. Pennacchioni
Validation: A. Camacho, N. Mancktelow, G. Pennacchioni
Visualization: G. Toffol
Writing – original draft: G. Toffol

Depth of Ancient Seismicity Along the Woodroffe Thrust (Central Australia): Constraints From Pseudotachylytes in Peraluminous Gneisses

G. Toffol[1,2], A. Camacho[3], N. Mancktelow[4], and G. Pennacchioni[1]

[1]Dipartimento di Geoscienze, Università di Padova, Padova, Italy, [2]Now at School of Earth and Environmental Sciences, Cardiff University, Cardiff, UK, [3]Department of Earth Sciences, University of Manitoba, Winnipeg, MB, Canada, [4]Department of Earth and Planetary Sciences, ETH Zürich, Zurich, Switzerland

Abstract The Woodroffe Thrust (WT) is a regional-scale mylonitic shear zone that developed during the Petermann Orogeny (630–520 Ma) in lower to mid-crustal rocks of the Musgrave Ranges, central Australia. In the upper part the WT hosts the largest volume worldwide of tectonic pseudotachylytes (coseismic quenched frictional melts). The pseudotachylytes were only marginally reworked along the mylonitic belt marking the WT, which mainly derived from the footwall amphibolite-facies rocks. Mid-crustal conditions of deformation along a shallowly dipping (<6°) WT were previously inferred from estimates of the P-T conditions of mylonitization along a regional transect in the N-S direction of thrusting. However, the pressure estimates were subject to large uncertainties. To better constrain the ambient conditions of the ancient seismic faulting along the WT, we investigate pseudotachylytes within peraluminous gneisses, a rock type more sensitive to P-T changes in the range of interest. Microstructural analysis allows the sequence of minerals (corundum, sillimanite, cordierite, andalusite, kyanite and garnet) developed during melt quenching and subsequent solid-state growth to be established. Critical observations are the growth of andalusite during pseudotachylyte cooling, constraining faulting at <0.45 GPa, and of kyanite during the immediately following ductile reactivation of pseudotachylytes. Seismic faulting is inferred to have occurred at ambient conditions of ∼0.4 GPa and 450°C, that is at much shallower conditions than previously assumed. These new P-T estimates imply an inclination of 20–25° of the WT, if the main stage of seismic faulting and mylonitization along the WT were coeval.

1. Introduction

Pseudotachylytes are quenched frictional melts that record ancient seismic slip of exhumed faults. As such, pseudotachylytes provide fundamental information on earthquake mechanics and rock rheology (Di Toro et al., 2005; Maddock, 1983; Mancktelow et al., 2022; Menegon et al., 2017; Michalchuk et al., 2023; Pennacchioni et al., 2020; Pittarello et al., 2008; Sibson, 1975; Swanson, 1992; Toffol et al., 2024). Most pseudotachylytes are thought to have formed near the base of the brittle upper crust (Sibson et al., 2006). Nevertheless, pseudotachylytes have also been described in exhumed middle and lower crustal rocks (Austrheim & Boundy, 1994; Camacho et al., 1995; Hawemann et al., 2018; Menegon et al., 2017; Orlandini et al., 2019; Passchier, 1982; Pennacchioni & Cesare, 1997; Pittarello et al., 2012; White, 2012) and have been interpreted to have formed at higher temperature conditions and depths than the typical brittle-ductile transition (i.e., below ∼10–15 km depth), that is where rocks are expected to flow rather than fail seismically. Present-day representatives of such deep earthquakes occur, for example, in the Indian shield underthrusting Tibet (Bodin & Horton, 2004), in the foreland of the northern Alps (Deichmann & Rybach, 1989; Singer et al., 2014) and in rift systems (Albaric et al., 2009).

Deep-seated pseudotachylytes are mainly hosted in dry, strong rocks, typically high-grade lower continental crustal rocks (e.g., anorthosites, Menegon et al., 2017; granulites, Orlandini et al., 2019; gabbros, Pittarello et al., 2012), but also in dry mafic and ultramafic rocks deformed at high grade and eclogite facies conditions (Pennacchioni et al., 2020; Ueda, 2008). These dry rocks have been inferred to survive changes in metamorphic conditions at deep structural levels without undergoing re-equilibration, due to sluggish reaction kinetics, and are capable of building up the high differential stress necessary to yield seismically under high confining pressure (Campbell et al., 2020; Hawemann, Mancktelow, Pennacchioni, et al., 2019; Hawemann, Mancktelow, Wex, et al., 2019; Mancktelow et al., 2022; Toffol et al., 2022).

Writing – review & editing: G. Toffol, A. Camacho, N. Mancktelow, G. Pennacchioni

The use of pseudotachylytes associated with high-grade rocks to study seismicity at relatively deep structural levels requires the ambient P-T conditions of pseudotachylyte formation to be correctly established since pseudotachylytes may well represent a shallow overprint during exhumation. Assessing these ambient conditions is not trivial. Pseudotachylytes are quenched melts and their mineralogy mainly reflects the transient high temperature stage of magmatic crystallization during rapid cooling rather than the metamorphic assemblage stable at the host rock ambient conditions. Dry conditions may prevent both metamorphic re-equilibration and ductile deformation, which would be pertinent for the high temperature conditions and would enhance re-equilibration. The extreme reaction sluggishness of these dry rocks is exemplified by the local preservation of the quenched glass (e.g., Pennacchioni et al., 2020). Also, for many host rock compositions the mineral assemblage that develops in pseudotachylytes does not tightly constrain P-T conditions (e.g., Papa et al., 2023) and may be affected by the presence or absence of host-rock clasts acting as nucleation seeds (Papa et al., 2018).

Large volumes of pseudotachylytes are locally found along major tectonic shear zones which crosscut exhumed middle to lower crustal rocks and, therefore, potentially preserve an exceptional record of seismicity at depth. In this case, the correct estimate of the environment of pseudotachylyte formation becomes critical for the interpretation of these large-scale structures. The largest volume of tectonic pseudotachylyte worldwide marks the upper part of the Woodroffe Thrust (WT), Musgrave Ranges (Camacho et al., 1995), involving predominantly the granulite-facies rocks of the hanging wall. In the eastern Musgrave Ranges, the WT is exposed for ∼100 km along the E-W strike and ∼60 km along the top-to-north direction of thrusting. Wex et al. (2017) estimated the metamorphic conditions of mylonitization of the WT, along the exposed N-S transect at 1.0–1.3 GPa, 650°C in the south, and 0.8–1.1 GPa, ∼520–620°C (depending on the geothermometer calibration) in the north. The estimated ambient pressures along the transect were used to infer a shallow dip angle of ≤6° for the WT and the occurrence of low-angle (under-)thrusting at lower crustal levels. However, Wex et al. (2017) remarked that the pressures from the northern exposures were potentially overestimated by >0.3 GPa, which does not rule out the possibility that the northern section of the WT actually represents a relatively shallow level thrusting. In the present study we provide new constraints on the deformation environment of the WT by studying pseudotachylytes hosted in peraluminous felsic granulites of the hanging wall of the WT as a more sensitive lithology for determining P-T conditions. The pseudotachylytes and the host rocks contain Al_2SiO_5 polymorphs that allow both the resolution of the complex sequence of crystallization occurring during quenching of the frictional melt and a better estimate of the pressure of formation of the pseudotachylytes. The new pressure estimate, significantly lower than previously inferred values for the northern WT, impacts the reconstruction by Wex et al. (2017) of the regional thrust geometry and highlights the problem of obtaining reliable ambient conditions estimates of seismic faulting when investigating pseudotachylytes.

2. Geological Setting

The Proterozoic Musgrave Province, central Australia, is located at the junction between the North, West and South Australian Cratons, which amalgamated ∼1,300 Ma during the development of Rodinia (Myers et al., 1996). In the Musgrave Province several large mylonitic shear zones (Bell, 1978; Camacho et al., 1997; Edgoose et al., 2004; Major, 1970; Major & Conor, 1993; Scrimgeour et al., 1999) developed during the intracontinental Petermann Orogeny (630–520 Ma) (Camacho & Fanning, 1995; Camacho & McDougall, 2000; de Gromard et al., 2019; Maboko et al., 1992): the WT; the northern Davenport and Davenport shear zones; the Ferdinand shear zone; and the Mann Fault (Figure 1). All these structures contain large amounts of tectonic pseudotachylyte breccias. The most important of these shear zones, the WT, juxtaposed hanging-wall, granulite facies gneisses and granites (Fregon subdomain) against footwall upper-amphibolite facies gneisses and granites (Mulga Park subdomain) (Camacho & Fanning, 1995; Edgoose et al., 1993; Major, 1970; Major & Conor, 1993; Wex et al., 2017). Both subdomains were affected by metamorphism during the Musgravian Orogeny (ca. 1,200 Ma), and were then intruded by voluminous syn- to post-tectonic plutons (Pitjantjatjara Supersuite, Giles Complex) and swarms of dolerite dikes (referred to as the Alcurra and Amata Dolerite swarms) before the Peterman Orogeny at ca. 630–520 Ma (Camacho et al., 1997; Camacho & Fanning, 1995; de Gromard et al., 2019; Gray, 1978; Maboko et al., 1991; Major & Conor, 1993; Scrimgeour et al., 1999; Smithies et al., 2011; Wade et al., 2008). The Fregon and Mulga Park subdomains likely represent different crustal levels (deeper and shallower, respectively) of the same terrane, as suggested by the similarity in lithological composition (mainly quartzo-feldspatic gneisses and granitoids with metapelites, metadolerites and mafic gneisses) and in the structural and magmatic history (Camacho & Fanning, 1995; Scrimgeour et al., 1999). The granulites of the Fregon

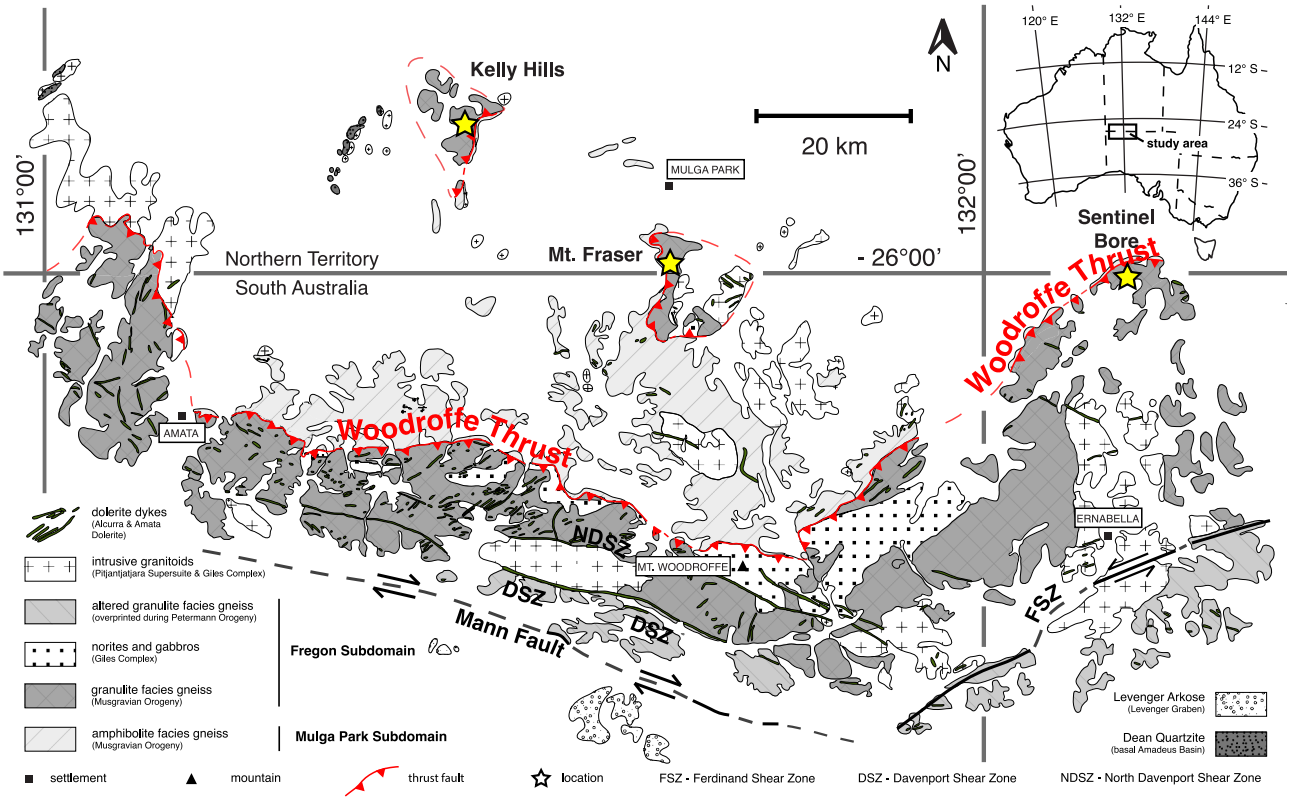

Figure 1. Geological map of the central Musgrave Block. Map modified after Wex et al. (2017). Yellow stars mark the locations of the studied samples in the WT.

subdomain experienced amphibolite-to sub-eclogite facies metamorphic conditions ranging from 700 to 750°C and 1.2–1.4 GPa (in the west) to 650–700°C and 1.2 GPa (in the east) (Camacho et al., 1997; Clarke et al., 1995; Ellis & Maboko, 1992; Scrimgeour & Close, 1999; White & Clarke, 1997). Ellis and Maboko (1992) interpreted these conditions to represent isobaric cooling during the Musgravian Orogeny and proposed exhumation along the WT as the last part of a long-lasting anticlockwise P-T-t path. In contrast, Camacho and McDougall (2000) and Camacho et al. (2009) reinterpreted the sub-eclogitic overprint as the product of a rapid cycle of burial and exhumation during the Petermann Orogeny.

The WT, well exposed in the eastern part of the Musgrave Ranges (e.g., Figure 2a), consists of a thick (100–600 m: Wex et al., 2018), currently gently south-dipping mylonitic zone associated with a pseudotachylyte-rich zone up to 1 km thick (Camacho et al., 1995). Mylonitization mainly affected the Mulga Park subdomain in the footwall (Camacho et al., 1995; Wex et al., 2018) while pseudotachylytes are concentrated in the upper part of the WT in hanging wall Fregon subdomain rocks. The more extensive mylonitization of the footwall was interpreted to result from the more hydrated conditions in the footwall rocks, which favoured weakening compared to the dry and strong granulites of the hanging wall (Bell, 1978; Camacho et al., 1995; Wex et al., 2018, 2019). The pseudotachylyte-rich zone comprises large volumes of pseudotachylyte (up to 4 vol %; Camacho et al., 1995), of which only a minor portion is mylonitised and hardly distinguishable from the footwall mylonites (Camacho et al., 1995; Wex et al., 2017, 2018).

3. Methods

Polished thin sections were studied by optical and scanning electron microscopy (SEM). SEM analysis with the FEG-SEM TESCAN Solaris at the Department of Geosciences of the University of Padova included back-scattered electron (BSE) imaging, energy dispersive spectroscopy (EDS), and electron backscattered diffraction (EBSD). High-resolution BSE imaging was performed using a mid-angle BSE detector at working conditions of 5 keV acceleration voltage, 300 pA beam current, and 3–5 mm working distance. EDS quantitative analyses were performed with a Ultim Max 65 (Oxford Instruments) detector, calibrated over Co, at working conditions of

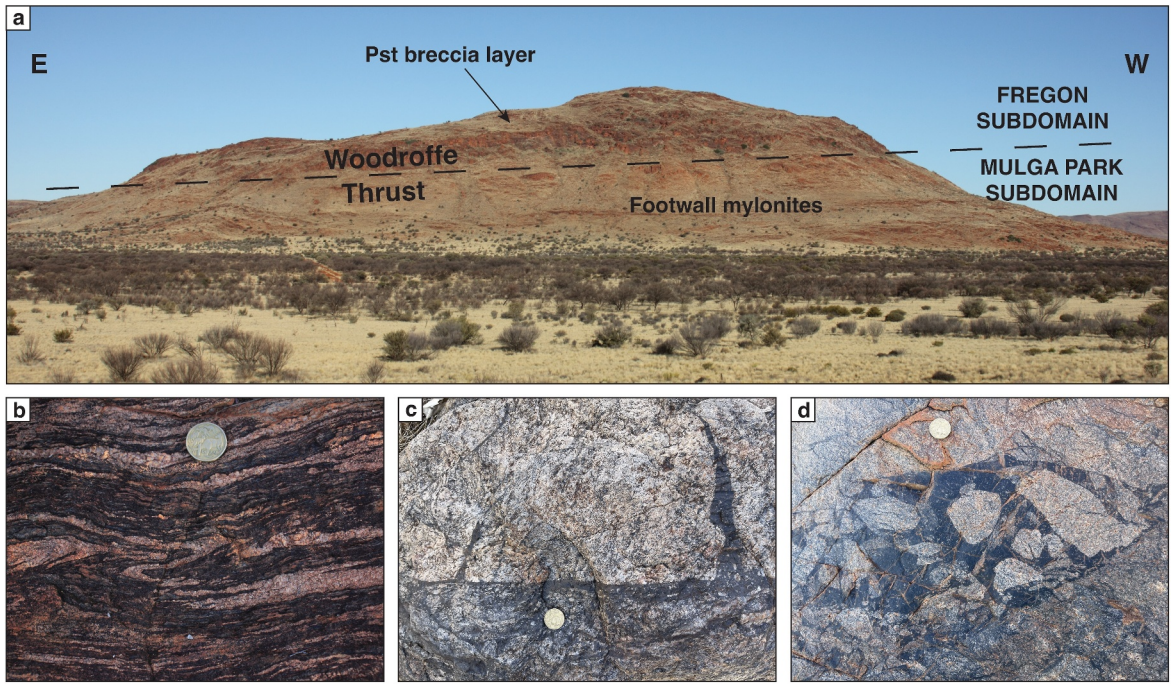

Figure 2. The Woodroffe Thrust. (a) View of Mount Fraser, looking towards south. The dashed black line marks the WT at the contact between the footwall mylonites and the pseudotachylyte breccia layer constituting the decametric cliff indicated by the black arrow. (b) Granulitic layering in a peraluminous gneiss. (c) Pseudotachylyte fault vein with a decimetric injection vein departing from it. (d) pseudotachylyte breccia. (b–d) Are from the upper section of the WT.

15 keV acceleration voltage, 3 nA beam current, and 5 mm working distance. EBSD maps were acquired with a CMOS-Symmetry II (Oxford Instruments) detector at working conditions of 15 keV acceleration voltage, 3 nA beam current, working distance 14–18 mm, and 70° sample tilt. The software Aztec and the MTEX 5.6.1 (Hielscher & Schaeben, 2008) toolbox of MATLAB® were used for EBSD indexing and post-processing. In EBSD maps, isolated indexed pixels were discarded and single, not-indexed pixels inside grains were filled with neighbour values. A threshold angle of 10° and a minimum of 2 indexed pixels were used for grain reconstruction. Raman spectroscopy was performed with a Horiba LabRAM HR Evolution Raman microscope (University of Pavia). A green (532 nm) laser with a spot size of approximately 1 μm was used. Spectra were obtained averaging two acquisitions of 5–15 s. Raman peaks of the investigated phases were identified by comparison with the RRUFF database. X-ray powder diffraction (XRPD) analysis was performed with a Panalytical X'Pert diffractometer (University of Padova). XRPD data were fitted using HighScore Plus with the built-in library of phases. X-ray fluorescence spectrometry (XRF) investigations were performed with a WDS Panalytical Zetium (University of Padova) on the same powders prepared for XRPD.

4. Samples

The pseudotachylyte-bearing samples come from 3 different localities along the WT in the eastern Musgrave Range shown in Figure 1: (a) Sentinel Bore (SB), (b) Mt. Fraser (FR) and (c) Kelly Hills (KH). These localities are ~80 km apart along the WT strike (E-W) direction and KH is ~20 km further N, compared to SB and FR, in the thrusting (N-S) direction.

In all three localities the host rock is similar and consists of medium-grained, felsic, peraluminous gneisses typically distinguished by a cm-to mm-thick banded structure of alternating, quartz-feldspar (light colour) and cordierite-sillimanite-rich (dark colour) layers (Figure 2b). Variable amounts of garnet, magnetite, ilmenite and biotite are preferentially distributed in the dark layers. XRPD mineralogical compositions and XRF bulk-rock chemical compositions of representative samples are reported in Figure S1 and in Table S1 in Supporting Information S1.

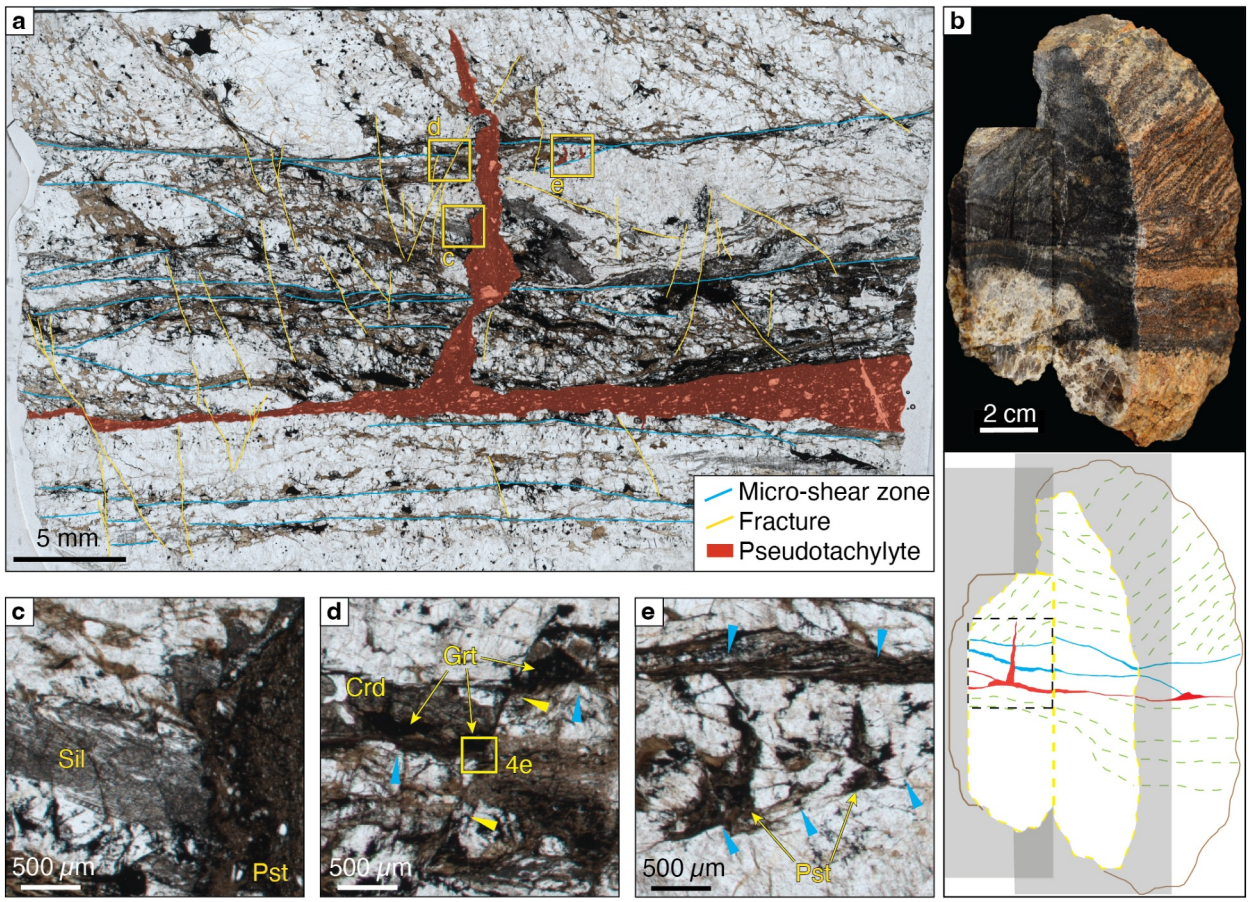

Figure 3. Sentinel Bore pseudotachylyte sample. (a) Thin section of pseudotachylyte fault and injection veins. Micro-shear zones and fractures are marked. (b) Sample from which the thin section was obtained. The sketch highlight the main pseudotachylyte vein and the micro-shear zones. The sample was cut perpendicular to both the fault and injection veins, that is roughly containing the slip vector. (c) Layer of fractured sillimanite cut by the pseudotachylyte injection vein. (d) Sharp fracture (yellow triangles) crosscutting micro-shear zone. (e) Detail of submillimetric injection veins departing from a micro-shear zone (blue triangles).

Pseudotachylytes (e.g., Figures 2c and 2d), widespread in the 3 localities, occur either as breccia layers of variable thickness (decimetric to metric) or as networks of mutually crosscutting, spatially dense, fault and injection veins (sensu Sibson, 1975). Portions of pseudotachylytes with the simplest geometry, with isolated fault veins and locally associated injection veins, were selected for investigations (Figure S2 in Supporting Information S1).

The sample from SB is a highly strained granulite including a mm-thick pseudotachylyte fault vein and an associated 2-cm-long injection vein (sample 18BJ46, Figures 3a and 3b). In this sample the main pseudotachylyte fault vein is discordant to the granulitic foliation on the side containing the injection vein, and parallel to the foliation on the other side. Adjacent to the pseudotachylyte the host rock exhibits pervasive microfractures and micro-shear zones oriented at a high angle and subparallel to the fault vein, respectively. The sample from FR (sample G22-29) includes a fault vein with a protruding injection vein. Samples from KH include a pluri-centimetric injection vein normal to the gneiss foliation (sample 18BJ63) and some isolated fault veins (sample 18–142).

5. Microstructural Observations

Microstructures of the host rock and pseudotachylytes in the three investigated localities show common features that are first presented here. Specific microstructures of the wall rock and the pseudotachylytes from the three localities are then described in the following subsections.

The melanosome layers include abundant prismatic sillimanite, 100's μm to a few mm long (Figure 3c), millimetric garnet and cordierite (Figure 3d), biotite in variable abundance and locally overgrown by kyanite, and

scattered magnetite and ilmenite. Sharp fractures, typically associated with the pseudotachylyte veins, are abundant and crosscut the original granulitic layering. Close to the pseudotachylytes these fractures are associated with sets of smaller fractures extending for only a few grains and decorated by micrometric opaque minerals. Sillimanite is strongly fractured throughout the entire host rock. There is no evidence of sillimanite recrystallization or break-down, not even along fractures. Instead, in contact with pseudotachylyte, sillimanite fragments show irregular shapes rimmed by quartz and these rims are corroded in contact with a homogenous matrix of K-feldspar (Figure 4a). Cordierite is commonly replaced by symplectites of andalusite, biotite and quartz along fractures proximal to a pseudotachylyte vein, while it is pristine away from it.

Pseudotachylyte veins contain survivor clasts and high temperature microlites (sillimanite, corundum and cordierite) in various proportions, together with aggregates of andalusite and a cryptocrystalline matrix enriched in Fe-oxide droplets.

5.1. SB Host Rock

The mm-sized cordierite is partly replaced along microfractures by a symplectite of andalusite, quartz and biotite. The vermicular quartz grains, arranged radially with respect to the microfractures, occur as inclusions in andalusite in the symplectite core and in biotite at the rim (Figures 4b and 4c). The microfractures are delineated by sub-micrometric magnetite, and by acicular kyanite (up to 20 μm long) preferentially aligned subparallel to the microfracture. Coarser kyanite locally overgrows the biotite in the symplectite (Figure 4c). K-feldspar in contact with reacted cordierite shows flame perthites.

The host-rock biotite is locally overgrown by randomly oriented prismatic kyanite, up to 50 μm long, arranged in sheaves (Figure 4d) and typically showing nanometric exsolution of magnetite along cleavage planes. The overgrown biotite contains clusters of sub-micrometric quartz grains aligned along the foliation. Granulite-facies corundum occurs inside large magnetite grains. Where not shielded by magnetite, corundum is corroded and associated with newly grown kyanite inside biotite.

Cauliflower-like dendritic garnet crystals, a few hundred micrometres in size, locally replace biotite (Figure 4d). The cauliflower microstructure results from the occurrence of vermicular inclusions of ilmenite locally arranged in radial patterns and by the locally preserved original texture of biotite. Kyanite and quartz, aligned along the foliation of the host biotite, are included by the new garnet. A micrometric rim of new garnet with euhedral facets also overgrows garnet where crosscut by fractures (Figure 4e).

Micro-shear zones, parallel to subparallel to the pseudotachylyte fault vein, occur within 2–3 cm distance from the vein and are irregularly spaced (Figure 3a). These shear zones either exploited the former foliation or link biotite-rich domains. The wider micro-shear zones locally show fractured and disaggregated grains. Some of these micro-shear zones were originally auxiliary rupture planes, as testified by the presence of submillimetric injection veins departing from one of them (Figure 3e). Abundant nanometric kyanite needles are aligned in the foliation of the micro-shear zones (Figures 4e and 4f), together with micrometric-sized quartz grains and biotite. The micro-shear zones are cut by the main pseudotachylyte injection vein and the associated sets of fractures that locally truncate and displace the kyanite foliation (Figures 3d and 4e).

5.2. SB Pseudotachylyte

The pseudotachylyte is largely crystallized, with subordinate portions of cryptocrystalline material of former residual melt. The mineral assemblage includes fine-grained (sub-micrometric to micrometric) quartz, andalusite, biotite, feldspar, sillimanite, kyanite, corundum, Fe-Ti oxides and garnet. The original quenched microstructure is mostly preserved in the injection vein, while it is partially sheared and disrupted due to vein-parallel shear in the fault vein. With the exception of cordierite and kyanite, the pseudotachylyte contains clasts of all the host-rock minerals, including low-melting point minerals such as K-feldspar and biotite.

Symplectite-like intergrowths (symplectite hereafter) of andalusite and quartz are common in the injection vein, locally surrounding a quartz clast nucleus (Figures 4g and 4h). The symplectite shows a variable relative abundance of andalusite and quartz but mostly consists of andalusite-hosted quartz vermicular inclusions. The shape of symplectites ranges from globular, close to the pseudotachylyte vein selvages (Figure 4g), to more irregular toward the vein centre. EBSD analysis indicates that andalusite of the symplectite is a single crystal and the quartz vermicular grains (or groups of neighbour vermicular grains) commonly have a crystallographic

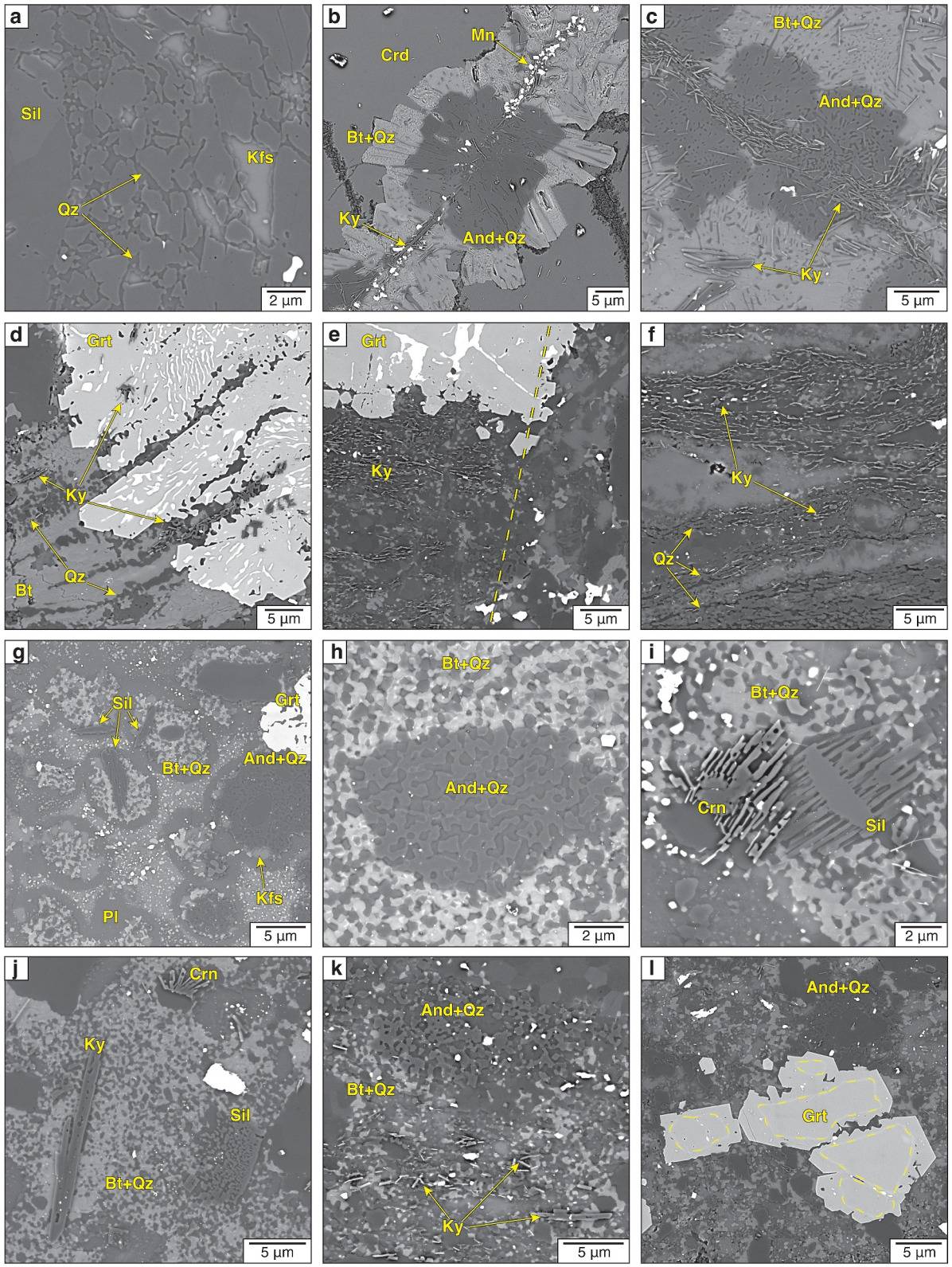
a
Sil
Kfs
Qz
2 µm
b
Mn
Crd
Bt+Qz
Ky
And+Qz
5 µm
c
Bt+Qz
And+Qz
Ky
5 µm
d
Grt
Ky
Qz
Bt
5 µm
e
Grt
Ky
5 µm
f
Ky
Qz
5 µm
g
Sil
Grt
And+Qz
Bt+Qz
Kfs
Pl
5 µm
h
Bt+Qz
And+Qz
2 µm
i
Bt+Qz
Crn
Sil
2 µm
j
Crn
Ky
Sil
Bt+Qz
5 µm
k
And+Qz
Bt+Qz
Ky
5 µm
l
And+Qz
Grt
5 µm

Figure 4.

orientation inherited from the seed quartz clasts (Figure 5). In many instances, andalusite in clustered symplectites has the same CPO and represents branches of the same arborescent 3D structure.

In the symplectite, andalusite is rimmed by an aggregate of submicrometric polygonal biotite, and the vermicular quartz is concomitantly recrystallized to small (~0.5 μm grain size) polygonal grains (Figure 4h). The contact between andalusite and biotite is sharp, and the symplectite microstructure is maintained. Biotite replacement is locally extensive to complete. The andalusite-quartz-biotite aggregates are typically rimmed by plagioclase associated with patches of K-feldspar (Figure 4g). These aggregates are immersed in a cryptocrystalline K-rich matrix clustered with nanometric Fe-Ti oxides.

Sillimanite microlites are common and form symmetric epitaxial overgrowths on sillimanite clasts (Figures 4i and 4j). They are needle-shaped (few microns in thickness and as much as 10 μm in length), elongated along the c-axis. In cross-section at a high angle to the c-axis, the microlites show a maze-shaped geometry with quartz filling the empty space. Acicular microlites of corundum occur as symmetric epitaxial overgrowths of corundum clasts and only locally as isolated needles with hopper shape (Figures 4i and 4j). Corundum microlites commonly show corrosion features resembling those of host-rock corundum. Kyanite crystals, resembling those overgrowing wall-rock biotite, are commonly found superimposed on the biotite-quartz symplectite aggregates (Figure 4j). The Raman spectra used to identify the Al_2SiO_5 polymorphs are reported in Figure S3 in Supporting Information S1.

Garnet grains with cauliflower shapes consist of a single crystal with minor internal lattice distortion (Figure 5). Neighbouring garnets share the same crystallographic orientation and belong to a single grain with an arborescent 3D structure (Figure S6 in Supporting Information S1). Garnet commonly includes abundant magnetite, delineating the cauliflower structure, as well as quartz and andalusite.

The injection vein shows a discontinuous internal foliation, at high angle to the vein selvages and to the vein-parallel flow structure, defined by the alignment of biotite-filled pressure shadows and elongated crystallized domains, mainly And-Qz-Bt symplectites (Figure S5 in Supporting Information S1). The fault vein shows an internal shear foliation parallel to the vein boundary and includes the same minerals as the injection veins. The pristine microstructure of the pseudotachylyte is disrupted, but locally quartz-andalusite-biotite symplectites are preserved (Figure 4k). Sillimanite microlites, locally surrounding sillimanite clasts, are less abundant than in the injection vein. Kyanite is more abundant, forming acicular crystals oriented in the shear plane, similar to kyanite in the micro-shear zones (Figure 4k). Locally kyanite occurs as more randomly oriented coarser crystals, resembling those in the host rock biotite (Figure 4k). Garnet is present close to host rock garnets whose fragments are dispersed in the pseudotachylyte (Figure 4l). The new garnet in the pseudotachylyte vein typically rims clasts; the clast-rim boundary is marked by a brighter nanometric layer in BSE images reflecting a sharp compositional variation or the presence of nanometric inclusions of oxides. Garnet grains are commonly elongated and boudinaged along the vein-parallel foliation, with the micro-boudinage necks filled with oxides. Pressure shadows around rigid clasts and large grains are filled with biotite.

5.3. FR Pseudotachylyte

The pseudotachylyte contains abundant microlites and clasts. The matrix is made of irregular aggregates of quartz and biotite, with minor plagioclase and cordierite and subordinate domains of cryptocrystalline material

Figure 4. Sentinel Bore, host rock and pseudotachylyte microstructures. BSE images of the host rock (a–f), pseudotachylyte injection vein (g–j) and fault vein (k–l). (a) Crushed sillimanite (Sil) close to a pseudotachylyte vein (Figure 3c). Sillimanite clasts are rimmed by quartz (Qz). (b) Cordierite (Crd) replaced, along a fracture marked by a trail of magnetite (Mn) grains, by a symplectite of andalusite (And), quartz and biotite (Bt). Quartz vermicules are continuous across the grain boundary between andalusite and biotite. Kyanite (Ky) needles of variable size cluster along the fracture. (c) Detail of cordierite replaced by andalusite-biotite-quartz symplectite with abundant kyanite. (d) Garnet (Grt) crystal overgrowing biotite. The structure of the biotite, with trails of micrometric euhedral quartz grains, is locally preserved in the garnet. Kyanite crystals overgrow biotite and are also included in garnet. Garnet contains abundant exsolutions of Fe-Ti oxides. (e) Sharp fracture displacing a micro-shear zone marked by the aligned submicrometric kyanite crystals and a garnet crystal (Figure 3d). Garnet is locally overgrown by a micrometric rim of new garnet with euhedral shapes along the fractured side and in contact with the micro-shear zone. (f) Micro-shear zone with abundant micrometric kyanite crystals parallel to the foliation. (g) Group of globular symplectic aggregates of andalusite-biotite-quartz. The aggregates are rimmed by plagioclase (Pl) and K-feldspar (Kfs); an unresolvable matrix rich in oxides fills the remnant space. Sillimanite microlites are present. (h) amoeboid andalusite-quartz symplectite surrounded by biotite and quartz. The andalusite-biotite boundary is sharp, and quartz is continuous through it. Where biotite replaces andalusite quartz is recrystallized to a polygonal aggregate. (i) Sillimanite and corundum (Crn) microlite barbs symmetrically and epitaxially overgrown on parent clasts. (j) Kyanite crystal overgrows the quartz-biotite matrix. Nanometric magnetite is exolved along the kyanite cleavage. (k) Partially disaggregated quartz-andalusite-biotite symplectite. Kyanite crystals are oriented parallel to fault vein. (l) Garnet clasts overgrown by new garnet. The clast boundary (highlighted with a yellow dashed line) is marked by bright nanometric layer.

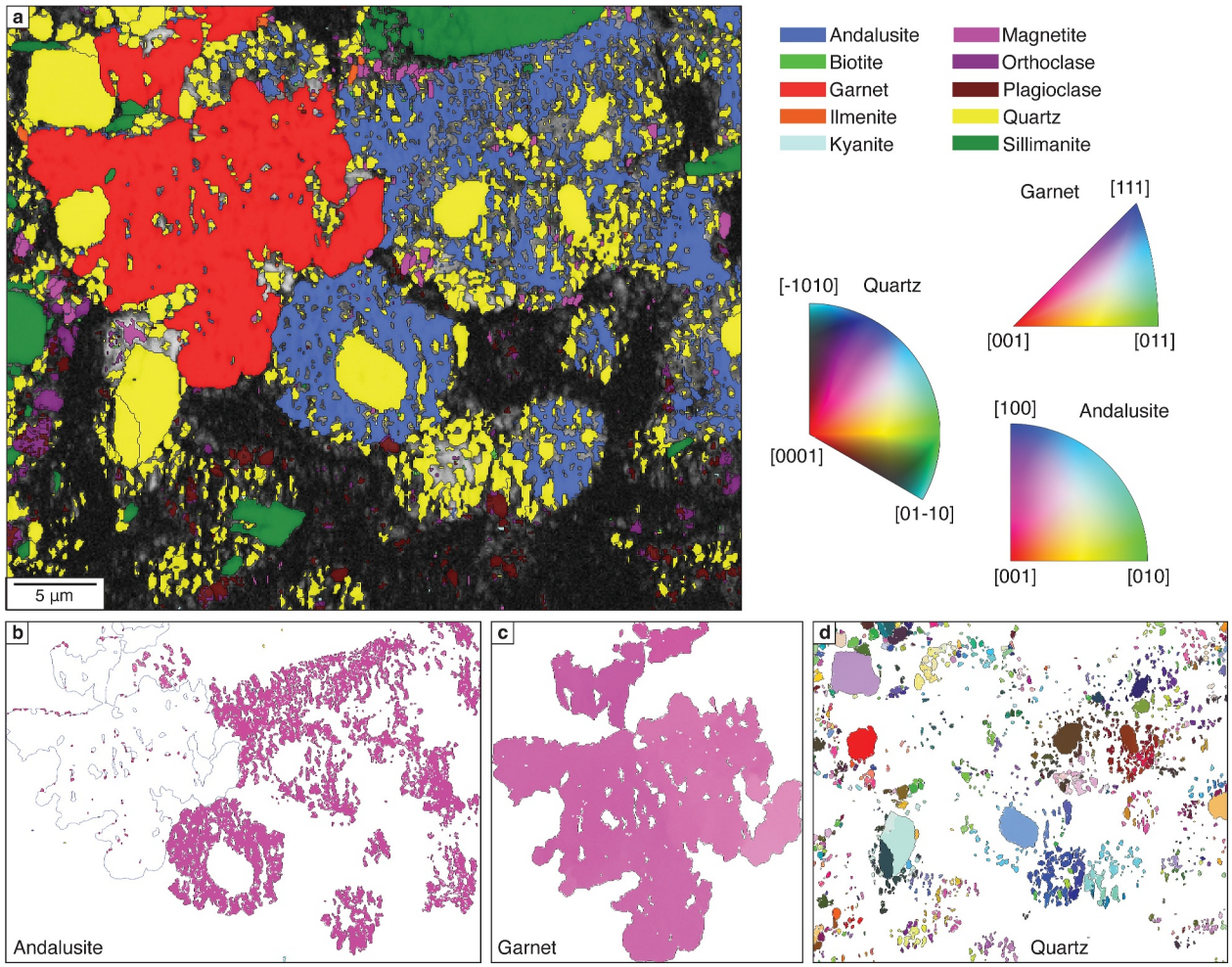

Figure 5. EBSD map in a pseudotachylyte injection vein from Sentinel Bore. (a) Phase map. (b) Andalusite orientation map. All the andalusite grains in the map have the same crystallographic orientation, meaning that they constitute a single dendritic crystal. Garnet grain boundary is outlined in blue for reference. (c) Garnet orientation map. The garnet is a single crystal. (d) Quartz orientation map. The crystallographic orientation of small quartz vermicules within andalusite is controlled by that of quartz clasts nearby. Colour coding of the orientation maps, based on the inverse pole figures with respect to *z*-direction.

disseminated with nanometric oxides droplets. Microlites of sillimanite are abundant as symmetric epitaxial overgrowths of sillimanite clasts showing the typical lozenge- to maze-shaped pattern in cross sections (Figures 6a–6c). Corundum prismatic microlites, a few micrometres in size and recognisable by their typical corrosion features, are widespread, either isolated or surrounding corundum clasts (Figures 6b and 6c). Kyanite is present as micrometric acicular crystals. In the sample G22-29, small (few mm in size) grains of andalusite were locally identified in EBSD maps nearby or in contact with sillimanite. The grains indexed as andalusite by EBSD are rounded in shape, locally with small irregular quartz inclusions (Figure 6d; Figure S6 in Supporting Information S1), which, in contrast to the sample 18BJ46 from SB, do not form the typical symplectite aggregates well recognizable already in BSE images. Host-rock garnet crosscut by the pseudotachylyte is shattered and healed by a rim (brighter in BSE images) of new garnet (Figure 6e). In proximity to the host rock garnet, small garnet clasts are overgrown by a euhedral garnet rim. Host-rock plagioclase crosscut by a pseudotachylyte injection vein is intruded by small (up to 20 µm in length) subsidiary injection veins departing from the principal one (Figure 6f). These injections, only a couple of microns in thickness, are filled with submicrometric, elongated and lozenge-shaped microlites, most likely sillimanite and corundum.

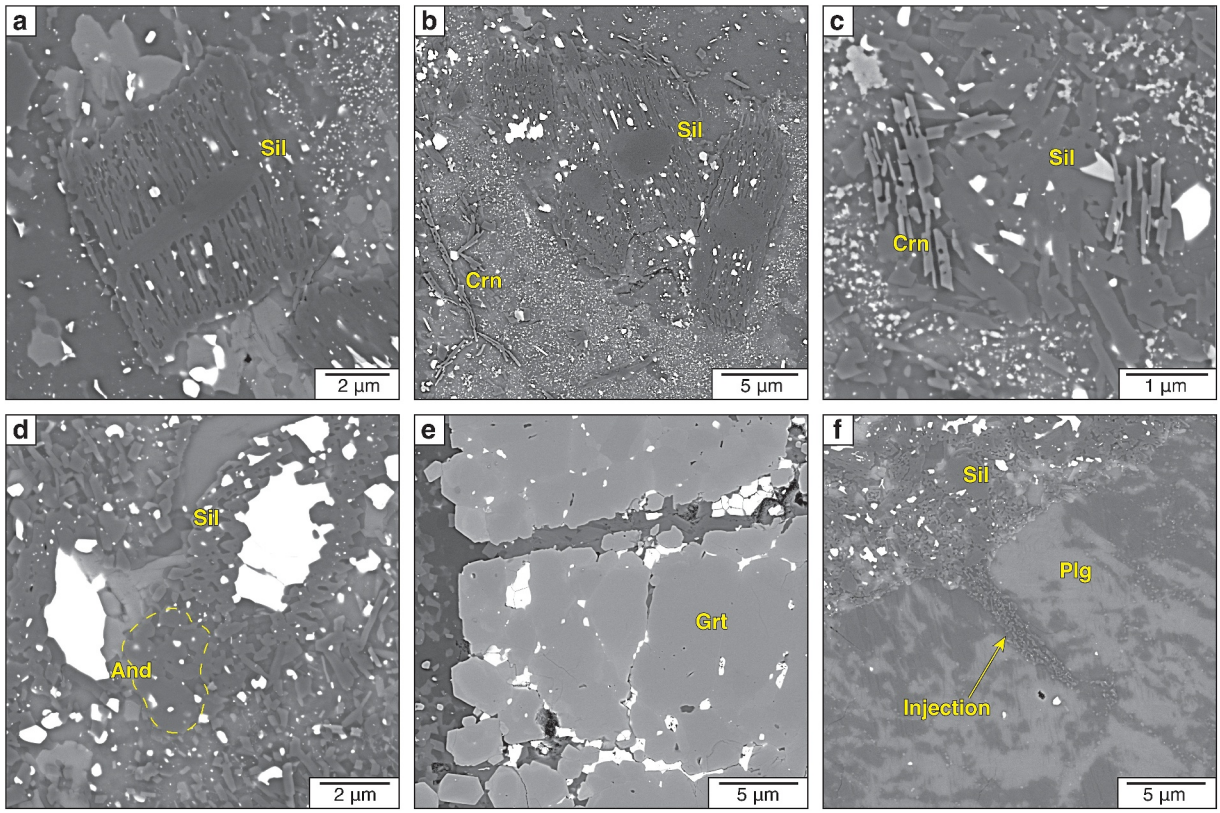

Figure 6. Mount Fraser pseudotachylyte microstructures. (a) Sillimanite needle-shaped microlites symmetrically overgrowing a sillimanite clast. (b, c) Sillimanite microlites and micrometric corundum microlites with corroded features. (d) Micrometric andalusite crystals (marked with a dashed yellow line) in contact with sillimanite microlites (see Figure S6 in Supporting Information S1 for the EBSD phase map) (e) healed cataclastic garnet at the selvage of the pseudotachylyte injection vein. The fragments are highlighted by a light-colour halo. (f) Small injection vein departing perpendicular from the main injection vein. The vein includes abundant sillimanite.

5.4. KH Host Rock and Pseudotachylyte

Cordierite is abundant and typically replaced by both sheaves of acicular kyanite associated with abundant magnetite, quartz, and scarce biotite (Figure 7a), and by andalusite-bearing symplectites similar to those observed in the SB locality (Figure 7b). Biotite in the host rock is rare. The sample 18BJ63 includes a pristine pseudotachylyte injection vein mostly composed of a homogeneous cryptocrystalline matrix with sparse droplets of oxides. Clasts of the host rock minerals are not abundant and microlites are less abundant than in the other investigated samples. Epitaxial microlite barbs of sillimanite symmetrically overgrow sillimanite clasts (Figure 7c). Microlitic cordierite occurs as globular symplectite-like intergrowths with rounded to vermicular quartz commonly including quartz or sillimanite clasts (Figure 7d; Figure S7 in Supporting Information S1). Micrometric acicular kyanite is scattered throughout the pseudotachylyte (Figure 7e). Cauliflower garnet is absent, but the finest grains of pulverised host-rock garnet in contact to the pseudotachylyte show a micrometric euhedral rim of new garnet (Figure 7f).

6. Mineral Chemistry

Chemical compositions of cordierite (Figure 8), garnet and, where relevant, other phases of the studied samples are summarized here and available in the repository. Compositions of the small microlites may be spurious due to contamination by other phases.

Sentinel Bore—Host rock cordierite has a (Mn/(Fe + Mg + Mn) ratio of ~0.1. Ilmenite contains up to 10 wt% MnO. Garnet is rich in Mn and Fe with an average composition of spessartine 44.9%, almandine 39.1%, pyrope 13.7% and grossular 2.3%. Granulite-facies biotite contains about 2.4–3.4 wt% TiO_2 and up to 0.5 wt% of MnO. Biotite derived from breakdown of cordierite is Ti-free and contains less Fe and slightly more Mg than granulite-

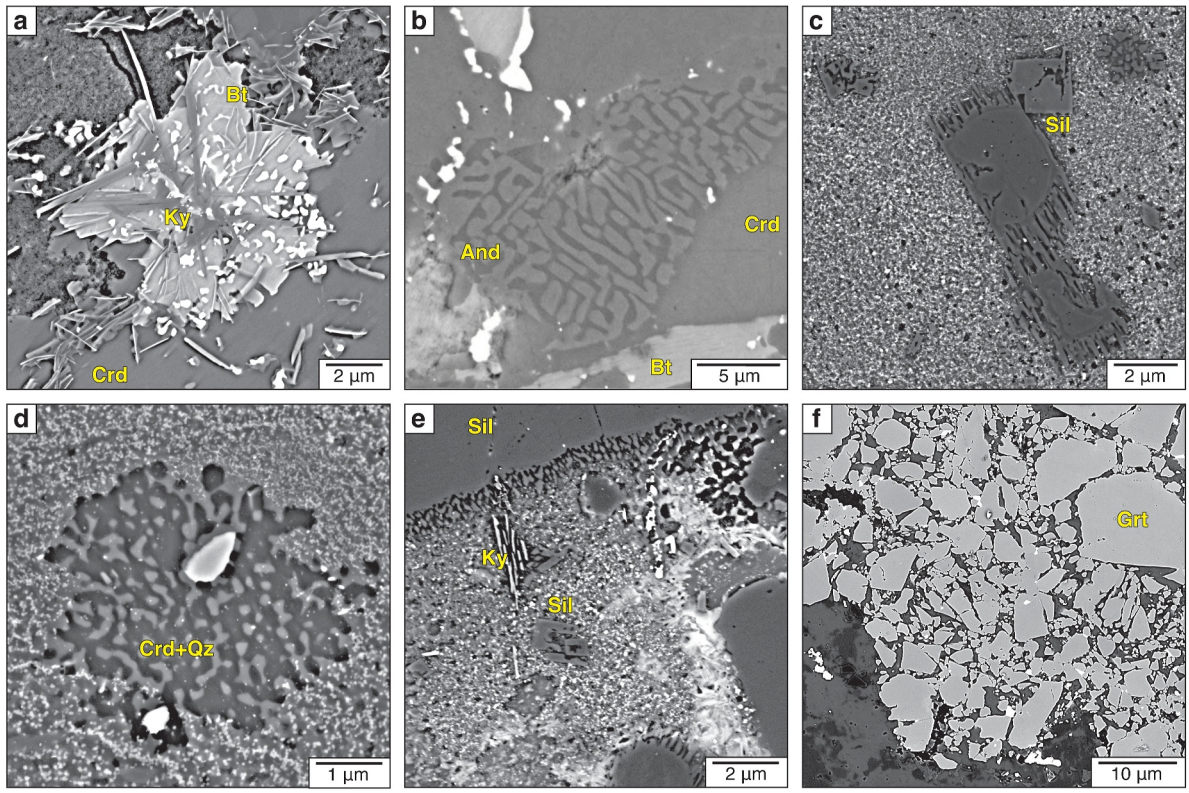

Figure 7. Kelly Hills host-rock and pseudotachylyte microstructures. (a) Host-rock cordierite replaced by quartz, biotite, kyanite and magnetite. (b) Andalusite-quartz symplectite replacing cordierite in the host rock. (c) Sillimanite microlites in a pseudotachylyte vein with unresolvable matrix. (d) Cordierite microlite intergrowth with quartz. (e) Micrometric kyanite crystals in contact with sillimanite microlites. (f) Cataclastic garnet at the selvages of a pseudotachylyte fault vein.

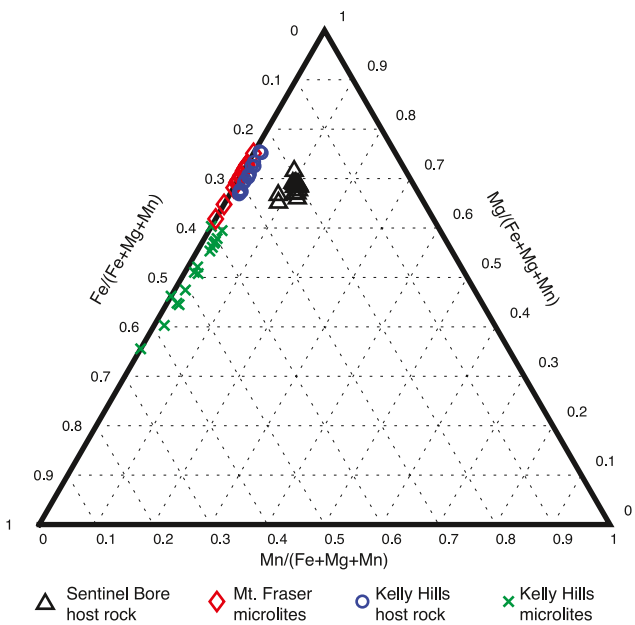

Figure 8. Cordierite compositions. Ternary plot showing the relative abundance of Fe, Mg, and Mn in cordierites from the host-rock and the pseudotachylytes.

facies biotite (on average 7.5 and 9.7 wt% FeO and 17.9 and 16.9 wt% MgO, respectively). Andalusite contains about 1 wt% of FeO and no MnO.

Mount Fraser—Cordierite crystallised in the pseudotachylyte contains no Mn and has average Fe/(Fe + Mg + Mn) of ~0.3. Granulite-facies garnet has an average composition of almandine 62.5%, pyrope 31.5%, spessartine 2.6% and grossular 3.4% and is not significantly different from the partially healed cataclastic garnets in the pseudotachylyte.

Kelly Hills—Cordierite has very low Mn content: Mn/(Fe + Mg + Mn) < 0.02. There is a variation in Mg and Fe ratios in host-rock cordierites and cordierites crystallizing from the pseudotachylyte, with the latter richer in iron and poorer in Mg (on average Fe/(Fe + Mg + Mn) ~0.29, Mg/(Fe + Mg + Mn) ~0.71 and 0.48, 0.52 for host-rock cordierites and microlitic cordierites respectively). Garnet is Fe-rich, with average composition of almandine 59.3%, pyrope 26.1%, spessartine 11.5% and grossular 3.1%.

7. Discussion

7.1. Crystallization Sequence in the Pseudotachylyte

The mineral assemblage of a deep-seated pseudotachylyte, developed under metamorphic conditions, potentially consists of: (a) microlites of high melting point minerals that directly crystallize from the quenched melt; (b) devitrification products that develop after cooling below the glass transition temperature T_g (i.e., the temperature at which melt viscosity is $\sim 10^{13}$ Pas, depending upon chemistry and cooling rate and typically >800°C for silicate

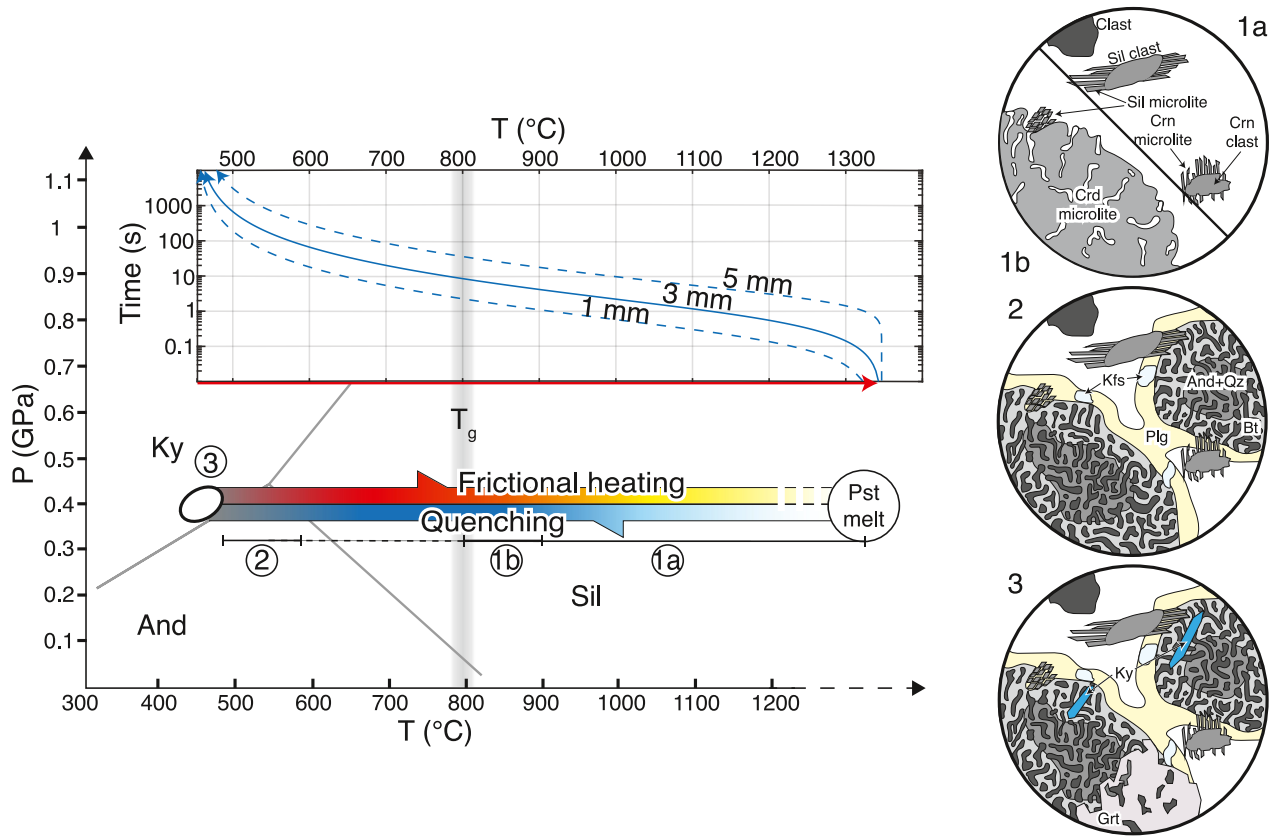

Figure 9. Scheme of the mineralogical evolution of SB pseudotachylyte injection vein. The P-T diagram, showing the fields of stability of andalusite, kyanite and sillimanite, includes the inferred thermal evolution associated with the development of frictional melts. This evolution is linked to the sequence of mineral growth determined in the peraluminous pseudotachylyte. We distinguish four stages of mineral growth during the progressive cooling of the frictional melt at the ambient temperature illustrated in the circles to right of the figure: (1a) growth of sillimanite and corundum microlites at $T > T_g$; (1b) growth of cordierite microlite at $T < 900°C$ until $T = T_g$; (2) replacement of microlitic cordierite by andalusite-quartz-biotite symplectite when the pseudotachylyte enters the stability field of andalusite and approaches ambient conditions; (3) static growth of kyanite and garnet. Temperature evolution of the pseudotachylyte as a function of time is presented after modelling of cooling by thermal diffusion of a 1, 3, and 5 mm thick injection veins at an initial temperature of 1350°C (see Supporting Information S1 for details).

melts (Richet & Bottinga, 1986)); (c) metamorphic minerals that grow after cooling at the ambient P-T conditions.

In the following sections, we use the sequence of mineral crystallization, determined by microstructural analysis, and the stability fields of aluminosilicates and cordierite in pseudotachylyte and host rock, to establish the ambient conditions of deformation during and after frictional melting. We focus on the pseudotachylytes from SB locality, where different Al_2SiO_5 polymorphs (sillimanite, andalusite and kyanite) grew in a well-defined sequence that is linked to the pseudotachylyte cooling as summarized in Figure 9.

7.1.1. Crystallization From the Frictional Melt: Growth of Sillimanite and Corundum

Sillimanite and corundum microlites crystallized from the melt (Figure 4i). Both minerals have very high melting temperatures of 1400°C and 2000°C, respectively (Spray, 2010) and survived the melting process, resulting in abundant survivor grains commonly seeding microlite nucleation. Aluminosilicate microlites have been reported in peraluminous pseudotachylytes developed over a wide range of P-T conditions (e.g., Altenberger et al., 2013; Menant et al., 2018; Moecher & Brearley, 2004; Papa et al., 2023; Uijee et al., 2007). It is of note that sillimanite microlites have been described in pseudotachylytes formed at upper crustal levels (e.g., Papa et al., 2023) and, therefore, reflect the high temperature transient anomaly of frictional melt rather than high grade ambient conditions. Other high-T phases (e.g., mullite: Moecher & Brearley, 2004; Ujiie et al., 2007; Hercynite: Menant et al., 2018, Papa et al., 2023) were not identified in the pseudotachylyte.

7.1.2. Cooling of Solidified Pseudotachylyte: Growth of Andalusite-Bearing Symplectites

Andalusite-biotite-quartz aggregates in the pseudotachylyte (Figures 4g and 4h) resemble the symplectites replacing cordierite along fractures in the adjacent host rock (Figures 4b and 4c). In the pseudotachylyte, the symplectites commonly surround a quartz clast that apparently acted as nucleation seed and imparted the crystallographic orientation to vermicular quartz grains. Microstructures in the pseudotachylyte injection vein preserve ellipsoidal-shaped symplectites with cryptocrystalline patches in between, which are interpreted as a pristine pseudotachylyte microstructure of globular grains and interstitial melt. However, it is unlikely that the current symplectite corresponds to the pristine mineralogy considering the P-T stability field of andalusite (Figure 9) and that seismic faulting presumably occurred at a depth of at least the base of the brittle crust (i.e., 10 km or deeper). For this depth, the temperature for andalusite crystallization is ≤600°C, that is much lower than the T_g for which the frictional melt should have been largely solidified.

We propose that the andalusite-bearing symplectites replaced previous globular microlites of cordierite precipitated during the high temperature stage of quenching of the frictional melt. Ambient pressure, high temperature (>900°C) experiments on cordierite melt show that, during quenching, nucleation and growth of cordierite microlites is rapid (e.g., Fokin & Zanotto, 1999). Globular cordierite microlites have also been reported in upper-crustal pseudotachylytes within sillimanite-garnet-rich paragneisses from Calabria, southern Italy (Papa et al., 2023). Microlites of cordierite, resembling the andalusite-biotite-quartz symplectites, are also present in the pseudotachylyte from KH locality (Figure 7d). We infer that cordierite, crystallized at high temperature, was rapidly replaced by andalusite-biotite-quartz symplectites during cooling at <~550°C—a reference average lower boundary of cordierite stability field (Seifert & Schreyer, 1970). Cordierite replacement in the pseudotachylyte was accompanied by replacement of the metastable host-rock cordierite promoted by the pseudotachylyte-producing thermal transient. The replacement was mainly localized along the seismically induced microfracture network that also increased the reactive surface area by comminution and facilitated element diffusion and fluid remobilization. The replacement reaction of cordierite as defined by Vernon (1978) is $3Crd + 2Kspar + 2H_2O = 6Als + 2Bt + 9Qz$. Potassium required to produce biotite, is provided by the surrounding K-feldspar in the host rock or by the K-rich patches of now-devitrified glass in the pseudotachylyte. The absence of Ti in the symplectic biotite is consistent with its local crystallization from cordierite which is Ti-free. Magnetite can also be locally produced, particularly in the replaced host-rock cordierite, to account for excess Fe and balance the equation. Notably, cordierite breakdown is not observed in samples from outside the pseudotachylyte-rich zone of the WT (Figure S8 in Supporting Information S1). The link between replacement of host-rock cordierite and pseudotachylyte production recalls the very local re-equilibration of the host rock to ambient eclogite-facies conditions, limited to the pseudotachylyte veins and to the immediately surrounding damage zone, described in dry ophiolitic gabbros of the Lanzo Massif, western Alps (Pennacchioni et al., 2020). In the Fregon dry granulites, seismic fracturing and frictional heating likely remobilised aqueous fluids derived from biotite and cordierite, enhancing the reaction kinetics along the pathways of micro-fractures that triggered cordierite replacement.

7.1.3. Solid-State Deformation of Pseudotachylyte: Growth of Kyanite and Garnet

The sequential growth of kyanite and garnet, both in the host rock (Figures 4c and 4d) and pseudotachylyte (Figures 4j, 4k, and 5a), occurred after development of andalusite. Kyanite is abundant in all the samples as both small acicular crystals and coarser sheaves of prismatic crystals. The former are preferentially aligned along the foliation of the micro-shear zones and microfractures in the host rock, and along the fault-parallel foliation of the pseudotachylyte fault veins where andalusite symplectites are only locally preserved. Kyanite is also locally aligned into the weak foliation, crosscutting at high angle the injection vein, that is marked by biotite-filled pressure shadows surrounding clasts and andalusite-bearing symplectites. A critical observation is that the kyanite-bearing foliation of the micro-shear zones, subparallel to the main pseudotachylyte fault vein, is crosscut by the main pseudotachylyte injection vein that only shows an incipient foliation overprint (Figures 3d and 4e). These micro-shear zones exploited thin slip planes, as attested by the local occurrence of preserved micrometric protruding injection veins with a still preserved quenched microstructure. This suggests that solid-state deformation, localized to subsidiary thin pseudotachylyte veins that had rapidly cooled down to the ambient host rock temperature, occurred in the stability field of kyanite while frictional melt was still present in the nearby main slip zone that sequentially crystallized sillimanite, cordierite and andalusite during cooling. The evolution of a side-

wall rip-out type structure (Figure 3b), as described by Swanson (1989), provides a kinematic model for the progressive development and overprint between pseudotachylyte veins during an individual earthquake event.

The coarser kyanite is randomly oriented and preferentially overgrew biotite of the andalusite-biotite-quartz symplectites, similar to the host-rock kyanite sheaves overgrowing cordierite-replacing biotite and large biotite crystals.

Garnet in the injection vein includes andalusite and quartz grains (Figure 5) and resembles host-rock garnet overgrowing biotite and including kyanite crystals. Therefore, despite showing a cauliflower texture, which is commonly reported for microlites (Pittarello et al., 2015), garnet in the injection vein represents a metamorphic replacement of biotite similar to what takes place in the host rock. In contrast, the garnet rim overgrowing clasts within the pseudotachylyte fault vein crystallized during melt quenching. The new garnet is highlighted by the change in composition and by a bright rim at the contact with the clast, marked by a sharp increase in Fe or by growth of nanometric iron oxides.

7.2. P-T Ambient Conditions of Seismic Faulting Along the WT

The pressure conditions for the northern exposures of the WT were estimated by Wex et al. (2017) at 0.8–1.1 GPa by conventional geobarometry on the mylonites and were attributed also to the pseudotachylyte-rich layer above. The authors already noted that their pressure estimates may be overestimated by >0.3 GPa as a result of mineral compositions straddling the calibration ranges. In particular, while the relict plagioclase has oligoclase to andesine composition, the recrystallized plagioclase is more sodic, ranging from albite to oligoclase, with a trend to sodium-richer composition when moving from south to north. The Grt-Bt-Pl-Qz geobarometer of Wu et al. (2004) requires a plagioclase composition of An >17% (i.e., oligoclase or more calcic), so that pressure estimates of the more northerly samples are more prone to error. Furthermore, the Grt-Bt-Pl-Qz geobarometer of Wu et al. (2004) was only calibrated for metapelites, whereas the protolith of rocks considered in the study were generally mylonitised gneisses or granites. Also, kyanite considered for the Grt-Pl-Als-Qz geobarometer applied to the northern samples resulted from plagioclase breakdown and was not in equilibrium with the rest of the assemblage, as evidenced by the presence of relict sillimanite.

The mineralogy and microstructure of pseudotachylytes in peraluminous felsic granulites provides substantial new information to establish the ambient conditions of seismic deformation in the WT. Kyanite and andalusite have not been previously reported in the northern parts of the WT that are considered here. Wex et al. (2018) reported the occurrence of kyanite, derived from breakdown of plagioclase, in the WT felsic mylonites further to the south than the 3 localities studied here. The new discovery of andalusite in the pseudotachylyte and along seismically produced fractures constrains the ambient pressure of seismic faulting to ≤0.45 GPa (~15 km depth), considering the Al_2SiO_5 phase diagram of Pattison (1992), and Cesare et al. (2003). Potentially, the stability field of andalusite could expand toward higher P-T conditions by Mn^{3+} substitution of Al^{3+} (Abs-Wurmbach et al., 1983), but the analysed andalusite is Mn-free. The presence of andalusite in rocks where granulite facies sillimanite did not invert to andalusite also precludes the possibility that andalusite grew metastably (e.g., Ballevre et al., 1997). Consequently, we infer that the andalusite-biotite-quartz symplectites represent an equilibrium assemblage during the seismic thermal transient. The transient equilibrium conditions cannot be related to coseismic underpressure (Reches & Dewers, 2005). This would imply an almost instantaneous growth of andalusite-bearing symplectites, which also requires K diffusion from the surroundings and is thus considered to be unrealistic. Conversely, the thermal transient provides enough time (at least a few minutes, potentially considerably longer in the pseudotachylyte-rich portions of the WF) to crystallize andalusite.

Pseudotachylytes from the KH locality still contain cordierite microlites with a composition of Mg# ~0.5, which suggests a crystallization pressure ≤0.5 GPa (Holdaway & Lee, 1977; Newton & Wood, 1979), that is consistent with the growth of andalusite in the host-rock and with the pressure inferred for the other localities.

The occurrence of synkinematic kyanite in micro-shear zones exploiting thin pseudotachylytes, which are crosscut by coeval pseudotachylyte veins crystallizing andalusite (and cordierite), indicates that the maximum ambient temperature was ~550°C for the maximum inferred depth of faulting of ~15 km. Deformation in the micro-shear zones likely represents the effect of the mylonitization along the WT within the more competent rocks of the Fregon hanging wall. For WT deformation in the northern sectors, the temperature of mylonitization has been estimated by Wex et al. (2017) in the range between 460°C and 550°C, depending on the calibration used

for the garnet-biotite thermometer. A temperature of mylonitization lower than the most conservative estimate of 460°C seems unlikely considering the dynamic recrystallization mechanism of quartz by grain boundary migration and subgrain rotation and the relatively low strength of mylonites estimated by quartz paleopiezometry (Wex et al., 2019).

Therefore, considering the stability diagram of aluminosilicates (Figure 9), the ambient conditions of seismic faulting along the WT, at the latitude of the SB, MF and KH localities, were in the range of 460–550°C and 0.3–0.45 GPa at a depth of 10–15 km. However, assuming shallow faulting at 10 km and 450°C or 15 km and 550°C would result in an unrealistically high thermal gradient of 45°C/km, if the mylonitization and seismic faulting were coeval. This suggest that either faulting occurred at a depth of around 15 km at ca 450°C—with a still somewhat elevated thermal gradient of 30°C/km, compared to the 16–18°C/km estimated by Camacho et al. (1997) for the Musgrave Block—or seismic faulting and mylonitization were not coeval, with faulting predating ductile deformation before later burial and increase in temperature.

Therefore, the main imposing seismic events responsible for the development of the enormous volumes of pseudotachylytes towards the base of the Fregon hanging wall block along the WT occurred at shallower crustal levels (~450°C and 0.4 GPa) than previously suggested.

7.3. Geometry and Evolution of the Woodroffe Thrust

Previous pressure estimates constrained the WT to dip very gently at around 6° (Wex et al., 2017). The new estimated pressure of ≤0.45 GPa for the seismic faulting along the WT is instead consistent with a dip of ~20–25°—assuming an average rock density of 2700 kg/m^3, no relevant paleo-topography, and considering the distance of 60 km between the northernmost and southernmost outcrops, which, according to Wex et al. (2017), record pressures of 1.0–1.3 GPa. A dip angle of 20–25° is in line with the tipicall geometry of thrust faults (Anderson, 1951). Considering that KH locality is around 10 km further north in thrust direction compared to SB and FR localites, and that we estimate similar pressures in the three localities, a more complex geometry may exist in the northern section. Unfortunately, with our approach we cannot resolve this complexity.

The WT was active throughout the entire Petermann orogeny and potentially continued to localize deformation and guide exhumation of the Musgrave Province, still presenting sparse seismicity in present times (de Gromard et al., 2021). Despite its importance for the structural setting of the Musgrave Ranges, its evolution is still hard to decipher. The cyclical overprint of pseudotachylytes and mylonites locally observable in the mylonitic portions of the WT towards the pseudotachylyte-rich zone (Camacho et al., 1995; Wex et al., 2017) implies a coeval development of the structures at similar P-T conditions. Wex et al. (2017) suggested that the main volume of WT pseudotachylytes was produced along a crustal-scale seismic fault that preceded mylonitization and that the laterally continuous layer of pseudotachylytes later formed the regional plane of anisotropy required to localize mylonitization, which preferentially localized in the more hydrous footwall rocks (Wex et al., 2017, 2018). A non-coeval development of mylonites and pseudotachylytes, with the latter occurring syn- to post-mylonitisation during the exhumation along the WT towards shallower crustal levels was instead hypothesized by Lin et al. (2005). However, Camacho et al. (1995) already argued that the scarce presence of pseudotachylytes in the mylonite zone is in contradiction with this hypothesis, since a weak planar layer extending continuously for tens to hundreds of kilometres would represent the ideal precursor for earthquake rupture nucleation and propagation, such that pseudotachylytes should preferentially concentrate in the footwall mylonites rather than in the undeformed strong hanging wall. An in-depth discussion of the evolution of the WT is beyond the scope of this paper. We envisage that careful dating of seismically affected minerals embedded as clasts in the pseudotachylyte or in the immediate damage zones (similar to what was done by Zertani et al. (2024) on apatite from the pseudotachylyte-bearing plagioclase-rich rocks of Lofoten) may help untangle the conundrum.

8. Conclusions

The analysis of pseudotachylytes in lower crustal peraluminous gneiss of the Woodroffe Thrust hanging wall provides tight constraints on the ambient conditions of seismic faulting, locating it at much shallower crustal levels (~15 km of depth) than previously inferred for the northern portions of this major regional tectonic lineament. The microstructural analysis indicates a clear sequence of crystallization of aluminosilicates (sillimanite, cordierite, andalusite and kyanite) and at different stages of quenching of the frictional melt, thermal re-equilibration to the ambient conditions and ductile reactivation coeval with faulting. The development of (a)

andalusite during perturbed temperature conditions induced by frictional melting, (b) cordierite directly crystallized from the melt, and (c) kyanite crystallized along sites of solid-state deformation in micro-shear zones exploiting minor pseudotachylytes allow the ambient conditions of pseudotachylyte formation to be constrained at around 0.4 GPa and 450°C.

The Musgrave Ranges area is a prime example of exhumed dry lower crustal rocks deformed along different ductile shear zones, each containing huge volumes of tectonic pseudotachylytes. The reported occurrence of ductilely deformed pseudotachylytes in high-grade rocks has been considered as evidence for a relatively deep origin of seismic faulting similar to other examples of lower crustal rocks hosting pseudotachylytes (e.g., Menegon et al., 2021). These deep-seated pseudotachylytes have been used to investigate the mechanisms of deformation at mid- to lower-crustal levels and have been considered as representative of present-day seismicity at the base of the continental crust. However, our study indicates that pseudotachylytes hosted in lower crustal rocks are not necessarily developed at high-grade conditions, highlighting the importance of reliable estimates of ambient conditions when extrapolating field observations to processes.

Data Availability Statement

All the data utilized for this research is available at the repository published by Toffol et al. (2025).

Acknowledgments
J. Nava and M.C. Dalconi are acknowledged for help with SEM analyses. M. Gilio is acknowledged for help with Raman analysis. S. Masoch is acknowledged for discussion. We acknowledge comments by C. Rowe and an anonymous reviewer and editorial handling by F. Rossetti. GP and GT acknowledge funding from PRIN_2020 WPMFE9 (project: THALES). Open access publishing facilitated by Universita degli Studi di Padova, as part of the Wiley - CRUI-CARE agreement.

References

Abs-Wurmbach, I., Langer, K., & Schreyer, W. (1983). The influence of Mn^{3+} on the stability relations of the Al_2Si0_5 polymorphs with special emphasis on manganian andalusites (Viridines), $(Al_{1-x}\ Mn_x^{3+})_2(O/SiO_4)$: An experimental investigation. *Journal of Petrology*, *24*(1), 48–75. https://doi.org/10.1093/petrology/24.1.48

Albaric, J., Déverchère, J., Petit, C., Perrot, J., & Le Gall, B. (2009). Crustal rheology and depth distribution of earthquakes: Insights from the central and southern East African Rift System. *Tectonophysics*, *468*(1–4), 28–41. https://doi.org/10.1016/j.tecto.2008.05.021

Altenberger, U., Prosser, G., Grande, A., Günter, C., & Langone, A. (2013). A seismogenic zone in the deep crust indicated by pseudotachylytes and ultramylonites in granulite-facies rocks of Calabria (Southern Italy). *Contributions to Mineralogy and Petrology*, *166*(4), 975–994. https://doi.org/10.1007/s00410-013-0904-3

Anderson, E. M. (1951). *The dynamics of faulting and dyke formation with application to Britain*. Oliver & Boyd.

Austrheim, H., & Boundy, T. M. (1994). Pseudotachylytes generated during seismic faulting and eclogitization of the deep crust. *Science*, *265*(5168), 82–83. https://doi.org/10.1126/science.265.5168.82

Ballèvre, M., Hensen, B. J., & Reynard, B. (1997). Orthopyroxene-andalusite symplectites replacing cordierite in granulites from the Strangways Range (Arunta block, central Australia): A new twist to the pressure-temperature history. *Geology*, *25*(3), 215–218. https://doi.org/10.1130/0091-7613(1997)025<0215:oasrci>2.3.co;2

Bell, T. H. (1978). Progressive deformation and reorientation of fold axes in a ductile mylonite zone: The Woodroffe Thrust. *Tectonophysics*, *44*(1–4), 285–320. https://doi.org/10.1016/0040-1951(78)90074-4

Bodin, P., & Horton, S. (2004). Source parameters and tectonic implications of aftershocks of the Mw 7.6 Bhuj earthquake of 26 January 2001. *Bulletin of the Seismological Society of America*, *94*(3), 818–827. https://doi.org/10.1785/0120030176

Camacho, A., Compston, W., McCulloch, M., & McDougall, I. (1997). Timing and exhumation of eclogite facies shear zones, Musgrave Block, central Australia. *Journal of Metamorphic Geology*, *15*(6), 735–751. https://doi.org/10.1111/j.1525-1314.1997.00053.x

Camacho, A., & Fanning, C. M. (1995). Some isotopic constraints on the evolution of the granulite and upper amphibolite facies terranes in the eastern Musgrave Block, central Australia. *Precambrian Research*, *71*(1–4), 155–181. https://doi.org/10.1016/0301-9268(94)00060-5

Camacho, A., & McDougall, I. (2000). Intracratonic, strike-slip partitioned transpression and the formation and exhumation of eclogite facies rocks: An example from the Musgrave Block, central Australia. *Tectonics*, *19*(5), 978–996. https://doi.org/10.1029/1999tc001151

Camacho, A., Vernon, R. H., & Gerald, J. F. (1995). Large volumes of anhydrous pseudotachylyte in the Woodroffe Thrust, eastern Musgrave Ranges, Australia. *Journal of Structural Geology*, *17*(3), 371–383. https://doi.org/10.1016/0191-8141(94)00069-c

Camacho, A., Yang, P., & Frederiksen, A. (2009). Constraints from diffusion profiles on the duration of high-strain deformation in thickened crust. *Geology*, *37*(8), 755–758. https://doi.org/10.1130/G25753A.1

Campbell, L. R., Menegon, L., Fagereng, Å., & Pennacchioni, G. (2020). Earthquake nucleation in the lower crust by local stress amplification. *Nature Communications*, *11*(1), 1322. https://doi.org/10.1038/s41467-020-15150-x

Cesare, B., Marchesi, C., Hermann, J., & Gómez-Pugnaire, M. T. (2003). Primary melt inclusions in andalusite from anatectic graphitic metapelites: Implications for the position of the Al_2SiO_5 triple point. *Geology*, *31*(7), 573–576. https://doi.org/10.1130/0091-7613(2003)031<0573:pmiiaf>2.0.co;2

Clarke, G. L., Buick, I. S., Glikson, A. Y., & Stewart, A. J. (1995). Structural and pressure-temperature evolution of host rocks of the Giles Complex, western Musgrave Block, Central Australia: Evidence for multiple high-pressure events. *AGSO Journal of Australian Geology and Geophysics*, *16*(1/2), 127–146.

de Gromard, R. Q., Kirkland, C. L., Howard, H. M., Wingate, M. T., Jourdan, F., McInnes, B. I., et al. (2019). When will it end? Long-lived intracontinental reactivation in central Australia. *Geoscience Frontiers*, *10*(1), 149–164. https://doi.org/10.1016/j.gsf.2018.09.003

Deichmann, N., & Rybach, L. (1989). Earthquakes and temperatures in the lower crust below the northern Alpine foreland of Switzerland. *Properties and Processes of Earth's Lower Crust*, *51*, 197–213. https://doi.org/10.1029/gm051p0197

Di Toro, G., Nielsen, S., & Pennacchioni, G. (2005). Earthquake rupture dynamics frozen in exhumed ancient faults. *Nature*, *436*(7053), 1009–1012. https://doi.org/10.1038/nature03910

Edgoose, C. J., Camacho, A., Wakelin-King, G. A., & Simons, B. A. (1993). *1:250 000 geological map series explanatory notes. Kulgera SG 53–5*. (2nd ed.). The Northern Territory Geological Survey.

Edgoose, C. J., Scrimgeour, I. R., & Close, D. F. (2004). *Report 15: Geology of the Musgrave Block, Northern Territory*. The Northern Territory Geological Survey.

Ellis, D. J., & Maboko, M. A. H. (1992). Precambrian tectonics and the physicochemical evolution of the continental crust. I. The gabbro-eclogite transition revisited. *Precambrian Research*, *55*(1–4), 491–506. https://doi.org/10.1016/0301-9268(92)90041-L

Fokin, V. M., & Zanotto, E. D. (1999). Surface and volume nucleation and growth in TiO2- cordierite glasses. *Journal of Non-Crystalline Solids*, *246*(1), 115–127. https://doi.org/10.1016/S0022-3093(99)00007-1

Gray, C. M. (1978). Geochronology of granulite-facies gneisses in the western Musgrave Block, central Australia. *Journal of the Geological Society of Australia*, *25*(7), 403–414. https://doi.org/10.1080/00167617808729050

Hawemann, F., Mancktelow, N. S., Pennacchioni, G., Wex, S., & Camacho, A. (2019). Weak and slow, strong and fast: How shear zones evolve in a dry continental crust (Musgrave Ranges, Central Australia). *Journal of Geophysical Research: Solid Earth*, *124*(1), 219–240. https://doi.org/10.1029/2018jb016559

Hawemann, F., Mancktelow, N., Wex, S., Pennacchioni, G., & Camacho, A. (2019). Fracturing and crystal plastic behaviour of garnet under seismic stress in the dry lower continental crust (Musgrave Ranges, Central Australia). *Solid Earth*, *10*(5), 1635–1649. https://doi.org/10.5194/se-10-1635-2019

Hawemann, F., Mancktelow, N. S., Wex, S., Camacho, A., & Pennacchioni, G. (2018). Pseudotachylyte as field evidence for lower-crustal earthquakes during the intracontinental Petermann Orogeny (Musgrave Block, Central Australia). *Solid Earth*, *9*(3), 629–648. https://doi.org/10.5194/se-9-629-2018

Hielscher, R., & Schaeben, H. (2008). A novel pole figure inversion method: Specification of the MTEX algorithm. *Applied Crystallography*, *41*(6), 1024–1037. https://doi.org/10.1107/s0021889808030112

Holdaway, M. J., & Lee, S. M. (1977). Fe-Mg cordierite stability in high-grade pelitic rocks based on experimental, theoretical, and natural observations. *Contributions to Mineralogy and Petrology*, *63*(2), 175–198. https://doi.org/10.1007/bf00398778

Lin, A., Maruyama, T., Aaron, S., Michibayashi, K., Camacho, A., & Kano, K. I. (2005). Propagation of seismic slip from brittle to ductile crust: Evidence from pseudotachylyte of the Woodroffe Thrust, central Australia. *Tectonophysics*, *402*(1–4), 21–35. https://doi.org/10.1016/j.tecto.2004.10.016

Maboko, M. A. H., McDougall, I., Zeitler, P. K., & Williams, I. S. (1992). Geochronological evidence for ~530–550 Ma juxtaposition of two Proterozoic metamorphic terranes in the Musgrave Ranges, central Australia. *Australian Journal of Earth Sciences*, *39*(4), 457–471. https://doi.org/10.1080/08120099208728038

Maboko, M. A. H., Williams, I. S., & Compston, W. (1991). Zircon U-Pb chronometry of the pressure and temperature history of granulites in the Musgrave Ranges, Central Australia. *The Journal of Geology*, *99*(5), 675–697. https://doi.org/10.1086/629532

Maddock, R. H. (1983). Melt origin of fault-generated pseudotachylytes demonstrated by textures. *Geology*, *11*(2), 105–108. https://doi.org/10.1130/0091-7613(1983)11<105:moofpd>2.0.co;2

Major, R. B. (1970). Woodroffe Thrust zone in the Musgrave Ranges. *Quarterly Geological Notes/Issued by the Geological Survey of South Australia*, *35*, 9–11.

Major, R. B., & Conor, C. H. H. (1993). Musgrave block. In J. Drexel, W. V. Preiss, & A. J. Parker (Eds.), *Bulletin 54: The Geology of South Australia. Volume 1. The Precambrian* (pp. 156–167). Geological Survey of South Australia.

Mancktelow, N. S., Camacho, A., & Pennacchioni, G. (2022). Time-lapse record of an earthquake in the dry felsic lower continental crust preserved in a pseudotachylyte-bearing fault. *Journal of Geophysical Research: Solid Earth*, *127*(4), e2021JB022878. https://doi.org/10.1029/2021jb022878

Menant, A., Angiboust, S., Moni´e, P., Oncken, O., & Guigner, J. M. (2018). Brittle deformation during Alpine basal accretion and the origin of seismicity nests above the subduction interface. *Earth and Planetary Science Letters*, *487*, 84–93. https://doi.org/10.1016/j.epsl.2018.01.029

Menegon, L., Campbell, L., Mancktelow, N., Camacho, A., Wex, S., Papa, S., et al. (2021). The earthquake cycle in the dry lower continental crust: Insights from two deeply exhumed terranes (Musgrave Ranges, Australia and Lofoten, Norway). *Philosophical Transactions of the Royal Society A*, *379*(2193), 20190416.

Menegon, L., Pennacchioni, G., Malaspina, N., Harris, K., & Wood, E. (2017). Earthquakes as precursors of ductile shear zones in the dry and strong lower crust. *Geochemistry, Geophysics, Geosystems*, *18*(12), 4356–4374. https://doi.org/10.1002/2017gc007189

Michalchuk, S. P., Zertani, S., Renard, F., Fusseis, F., Chogani, A., Plümper, O., & Menegon, L. (2023). Dynamic evolution of porosity in lower-crustal faults during the earthquake cycle. *Journal of Geophysical Research: Solid Earth*, *128*(8), e2023JB026809. https://doi.org/10.1029/2023jb026809

Moecher, D. P., & Brearley, A. J. (2004). Mineralogy and petrology of a mullite-bearing pseudotachylyte: Constraints on the temperature of coseismic frictional fusion. *American Mineralogist*, *89*(10), 1486–1495. https://doi.org/10.2138/am-2004-1017

Myers, J. S., Shaw, R. D., & Tyler, I. M. (1996). Tectonic evolution of Proterozoic Australia. *Tectonics*, *15*(6), 1431–1446. https://doi.org/10.1029/96TC02356

Newton, R. C., & Wood, B. J. (1979). Thermodynamics of water in cordierite and some petrologic consequences of cordierite as a hydrous phase. *Contributions to Mineralogy and Petrology*, *68*(4), 391–405. https://doi.org/10.1007/bf01164524

Orlandini, O. F., Mahan, K. H., Williams, M. J., Regan, S. P., & Mueller, K. J. (2019). Evidence for deep crustal seismic rupture in a granulite-facies, intraplate, strike-slip shear zone, northern Saskatchewan, Canada. *Bulletin*, *131*(3–4), 403–425. https://doi.org/10.1130/b31922.1

Papa, S., Pennacchioni, G., Angel, R. J., & Faccenda, M. (2018). The fate of garnet during (deep-seated) coseismic frictional heating: The role of thermal shock. *Geology*, *46*(5), 471–474. https://doi.org/10.1130/g40077.1

Papa, S., Pennacchioni, G., Camacho, A., & Larson, K. P. (2023). Pseudotachylytes in felsic lower-crustal rocks of the Calabrian Serre massif: A record of deep-or shallow-crustal earthquakes? *Lithos*, *460*, 107375. https://doi.org/10.1016/j.lithos.2023.107375

Passchier, C. W. (1982). Pseudotachylyte and the development of ultramylonite bands in the Saint-Barthelemy Massif, French Pyrenees. *Journal of Structural Geology*, *4*(1), 69–79. https://doi.org/10.1016/0191-8141(82)90008-6

Pattison, D. R. (1992). Stability of andalusite and sillimanite and the Al2SiO5 triple point: Constraints from the Ballachulish aureole, Scotland. *The Journal of Geology*, *100*(4), 423–446. https://doi.org/10.1086/629596

Pennacchioni, G., & Cesare, B. (1997). Ductile-brittle transition in pre-alpine amphibolite facies mylonites during evolution from water-present to water-deficient conditions (Mont Mary nappe, Italian Western Alps). *Journal of Metamorphic Geology*, *15*(6), 777–791. https://doi.org/10.1111/j.1525-1314.1997.00055.x

Pennacchioni, G., Scambelluri, M., Bestmann, M., Notini, L., Nimis, P., Plümper, O., et al. (2020). Record of intermediate-depth subduction seismicity in a dry slab from an exhumed ophiolite. *Earth and Planetary Science Letters*, *548*, 116490. https://doi.org/10.1016/j.epsl.2020.116490

Pittarello, L., Di Toro, G., Bizzarri, A., Pennacchioni, G., Hadizadeh, J., & Cocco, M. (2008). Energy partitioning during seismic slip in pseudotachylyte-bearing faults (Gole Larghe Fault, Adamello, Italy). *Earth and Planetary Science Letters*, *269*(1–2), 131–139. https://doi.org/10.1016/j.epsl.2008.01.052

Pittarello, L., Habler, G., Abart, R., & Rhede, D. (2015). Garnet growth in frictional melts of the Ivrea Zone (Italy). *Italian Journal of Geosciences*, *134*(1), 149–161. https://doi.org/10.3301/ijg.2014.53

Pittarello, L., Pennacchioni, G., & Di Toro, G. (2012). Amphibolite-facies pseudotachylytes in Premosello metagabbro and felsic mylonites (Ivrea Zone, Italy). *Tectonophysics*, *580*, 43–57. https://doi.org/10.1016/j.tecto.2012.08.001

Reches, Z. E., & Dewers, T. A. (2005). Gouge formation by dynamic pulverization during earthquake rupture. *Earth and Planetary Science Letters*, *235*(1–2), 361–374. https://doi.org/10.1016/j.epsl.2005.04.009

Richet, P., & Bottinga, Y. (1986). Thermochemical properties of silicate glasses and liquids: A review. *Reviews of Geophysics*, *24*(1), 1–25. https://doi.org/10.1029/rg024i001p00001

Scrimgeour, I., & Close, D. (1999). Regional high-pressure metamorphism during intracratonic deformation: The Petermann Orogeny, central Australia. *Journal of Metamorphic Geology*, *17*(5), 557–572. https://doi.org/10.1046/j.1525-1314.1999.00217.x

Scrimgeour, I. R., Close, D. F., & Edgoose, C. J. (1999). *1:250,000 geological map series and explanatory notes. Petermann Ranges SG52-7* (2nd ed.). Northern Territory Geological Survey.

Seifert, F., & Schreyer, W. (1970). Lower temperature stability limit of Mg Cordierite in the range 1-7 kb water pressure: A redetermination. *Contributions to Mineralogy and Petrology*, *27*(3), 225–238. https://doi.org/10.1007/bf00385779

Sibson, R. H. (1975). Generation of pseudotachylyte by ancient seismic faulting. *Geophysical Journal International*, *43*(3), 775–794. https://doi.org/10.1111/j.1365-246x.1975.tb06195.x

Sibson, R. H., Toy, V. G., Abercrombie, R., & McGarr, A. (2006). The habitat of fault-generated pseudotachylyte: Presence vs. absence of friction-melt. *Geophysical Monograph-American Geophysical Union*, *170*, 153–166. https://doi.org/10.1029/170gm16

Singer, J., Diehl, T., Husen, S., Kissling, E., & Duretz, T. (2014). Alpine lithosphere slab rollback causing lower crustal seismicity in northern foreland. *Earth and Planetary Science Letters*, *397*, 42–56. https://doi.org/10.1016/j.epsl.2014.04.002

Smithies, R. H., Howard, H. M., Evins, P. M., Kirkland, C. L., Kelsey, D. E., Hand, M., et al. (2011). High-temperature granite magmatism, crust-mantle interaction and the Mesoproterozoic intracontinental evolution of the Musgrave Province, Central Australia. *Journal of Petrology*, *52*(5), 931–958. https://doi.org/10.1093/petrology/egr010

Spray, J. G. (2010). Frictional melting processes in planetary materials: From hypervelocity impact to earthquakes. *Annual Review of Earth and Planetary Sciences*, *38*(1), 221–254. https://doi.org/10.1146/annurev.earth.031208.100045

Swanson, M. T. (1989). Sidewall ripouts in strike-slip faults. *Journal of Structural Geology*, *11*(8), 933–948. https://doi.org/10.1016/0191-8141(89)90045-x

Swanson, M. T. (1992). Fault structure, wear mechanisms and rupture processes in pseudotachylyte generation. *Tectonophysics*, *204*(3–4), 223–242. https://doi.org/10.1016/0040-1951(92)90309-t

Toffol, G., Camacho, A., Mancktelow, N. S., & Pennacchioni, G. (2025). Depth of ancient seismicity along the Woodroffe Thrust (central Australia): Constraints from pseudotachylytes in peraluminous gneisses [Dataset]. *Research Data UniPD*. https://doi.org/10.25430/RESEARCHDATA.CAB.UNIPD.IT.00001625

Toffol, G., Pennacchioni, G., Menegon, L., Wallis, D., Faccenda, M., Camacho, A., & Bestmann, M. (2024). On-fault earthquake energy density partitioning from shocked garnet in an exhumed seismic midcrustal fault. *Science Advances*, *10*(9), eadi8533. https://doi.org/10.1126/sciadv.adi8533

Toffol, G., Yang, J., Pennacchioni, G., Faccenda, M., & Scambelluri, M. (2022). How to quake a subducting dry slab at intermediate depths: Inferences from numerical modelling. *Earth and Planetary Science Letters*, *578*, 117289. https://doi.org/10.1016/j.epsl.2021.117289

Ueda, T. (2008). Mylonitized ultramafic pseudotachylyte and associated deformation textures, Balmuccia peridotite massif, Ivrea Zone, Italy. In *AGU Chapman Conference on Shallow Mantle Composition and Dynamics 5th International Orogenic Lherzolite Conference (Mt. Shasta, California) Abstract Volume, 2008* (Vol. 79).

Ujiie, K., Yamaguchi, H., Sakaguchi, A., & Toh, S. (2007). Pseudotachylytes in an ancient accretionary complex and implications for melt lubrication during subduction zone earthquakes. *Journal of Structural Geology*, *29*(4), 599–613. https://doi.org/10.1016/j.jsg.2006.10.012

Vernon, R. H. (1978). Pseudomorphous replacement of cordierite by symplectic intergrowths of andalusite, biotite and quartz. *Lithos*, *11*(4), 283–289. https://doi.org/10.1016/0024-4937(78)90035-x

Wade, B. P., Kelsey, D. E., Hand, M., & Barovich, K. M. (2008). The Musgrave Province: Stitching north, West and South Australia. *Precambrian Research*, *166*(1–4), 370–386. https://doi.org/10.1016/j.precamres.2007.05.007

Wex, S., Mancktelow, N. S., Camacho, A., & Pennacchioni, G. (2019). Interplay between seismic fracture and aseismic creep in the Woodroffe Thrust, central Australia–Inferences for the rheology of relatively dry continental mid-crustal levels. *Tectonophysics*, *758*, 55–72. https://doi.org/10.1016/j.tecto.2018.10.024

Wex, S., Mancktelow, N. S., Hawemann, F., Camacho, A., & Pennacchioni, G. (2017). Geometry of a large-scale, low-angle, midcrustal thrust (Woodroffe Thrust, central Australia). *Tectonics*, *36*(11), 2447–2476. https://doi.org/10.1002/2017tc004681

Wex, S., Mancktelow, N. S., Hawemann, F., Camacho, A., & Pennacchioni, G. (2018). Inverted distribution of ductile deformation in the relatively "dry" middle crust across the Woodroffe Thrust, central Australia. *Solid Earth*, *9*(4), 859–878. https://doi.org/10.5194/se-9-859-2018

White, J. C. (2012). Paradoxical pseudotachylyte–Fault melt outside the seismogenic zone. *Journal of Structural Geology*, *38*, 11–20. https://doi.org/10.1016/j.jsg.2011.11.016

White, R. W., & Clarke, G. L. (1997). The role of deformation in aiding recrystallization: An example from a high-pressure shear zone, Central Australia. *Journal of Petrology*, *38*(10), 1307–1329. https://doi.org/10.1093/petroj/38.10.1307

Wu, C.-M., Zhang, J., & Ren, L.-D. (2004). Empirical Garnet-Biotite-Plagioclase-Quartz (GBPQ) geobarometry in medium- to high-grade metapelites. *Journal of Petrology*, *45*(9), 1907–1921. https://doi.org/10.1093/petrology/egh038

Zertani, S., Menegon, L., Whitehouse, M. J., Jeon, H., & Jamtveit, B. (2024). Dating fossil lower-crustal earthquakes by in-situ apatite U-Pb geochronology. *Earth and Planetary Science Letters*, *630*, 118621. https://doi.org/10.1016/j.epsl.2024.118621

References From the Supporting Information

Horai, K. I. (1971). Thermal conductivity of rock-forming minerals. *Journal of Geophysical Research*, *76*(5), 1278–1308. https://doi.org/10.1029/jb076i005p01278

Kanamori, H., Fujii, N., & Mizutani, H. (1968). Thermal diffusivity measurement of rock-forming minerals from 300 to 1100 K. *Journal of Geophysical Research*, *73*(2), 595–605. https://doi.org/10.1029/jb073i002p00595

Robie, R. A., & Waldbaum, D. R. (1968). *Thermodynamic properties of minerals and related substances at 298.150 K (25.00° C) and one atmosphere (1.013 bars) pressure and at higher temperatures* (Vol. 1259). US Government Printing Office.

Romine, W. L., Whittington, A. G., Nabelek, P. I., & Hofmeister, A. M. (2012). Thermal diffusivity of rhyolitic glasses and melts: Effects of temperature, crystals and dissolved water. *Bulletin of Volcanology*, *74*(10), 2273–2287. https://doi.org/10.1007/s00445-012-0661-6

Turcotte, D. L., & Schubert, G. (2002). *Geodynamics*. Cambridge University Press.